JOURNAL OF SPACECRAFT AND ROCKETS
Vol. 41, No. 5, September–October 2004

Supersonic Jet Impingement Navier–Stokes Computations for Vertical Launching System Design Applications

Kwang-Seop Lee* and Seung-Kyu Hong†
Agency for Defense Development, Taejon 305-600, Republic of Korea
and
Seung-O Park‡
Korea Advanced Institute of Science and Technology, Taejon 305-701, Republic of Korea

The jet impinging flow structure exhibits such complex natures as shock shell, plate shock, and Mach disk, depending on the flow parameters. The main parameters are the ratio of the jet pressure to the ambient pressure and the distance between the nozzle and the wall. Complexity and unsteadiness of this flow pose quite a numerical challenge for the flux-difference line of schemes, defying easy capture of the plate shock and recirculation zone at the jet center. Such difficulties are overcome and stable solutions are obtained first for jet impingement on a flat plate and then within a vertical launching system, yielding locations, as well as magnitudes of maximum pressure and heat flux for hardware designers. The plate shock and wall pressure beneath are found to oscillate with a frequency between 1 and 10 kHz, depending on the flow condition.

Nomenclature

$\tilde{A}, \tilde{B}, \tilde{C}$	=	Jacobian matrices in ξ, η, ϕ coordinates
D	=	nozzle exit diameter
$\bar{D}$	=	diagonal term
$\hat{F}, \hat{G}, \hat{H}$	=	flux vectors in general curvilinear coordinates
H	=	distance between nozzle exit and plate
I	=	identity matrix
J	=	Jacobian of the coordinate transformation
$\bar{M}, \bar{M}^{-1}$	=	transformation matrices between Q and $\tilde{Q}$
P, p	=	pressure
P_r	=	pressure ratio
P_t	=	chamber pressure
Q	=	conservative variable vector
$\tilde{Q}$	=	primitive variable vector
$\tilde{\tilde{Q}}$	=	characteristic variable vector
T_t	=	chamber temperature
$\bar{T}, \bar{T}^{-1}$	=	transformation matrices between $\tilde{Q}$ and $\tilde{\tilde{Q}}$
t	=	time
α	=	constant for time integration
Δ	=	difference
ΔQ	=	$\bar{M}\Delta\tilde{Q}$
$\Delta\tilde{Q}$	=	$\bar{M}^{-1}\Delta Q$
$\Delta\tilde{\tilde{Q}}$	=	$\bar{T}^{-1}\bar{M}^{-1}\Delta Q$
δ	=	time difference
ε	=	constant for shock fixing
Λ	=	diagonal matrix
λ	=	eigenvalue
μ	=	viscosity
ξ, η, ϕ	=	general coordinates
τ_w	=	shear stress on the wall, $\mu(\partial u/\partial y)$
∇	=	backward difference

Subscripts

j, k, l	=	indices for general coordinates
n	=	time level
w	=	wall
v	=	viscous term
τ	=	physical time

Superscripts

$-$	=	average
$\pm$	=	split condition

Received 4 December 2002; revision received 20 July 2003; accepted for publication 1 August 2003.

*Senior Researcher, Aerodynamics Branch.
†Head, Department of Missile Airframe and Launcher. Member AIAA.
‡Professor, Department of Aerospace Engineering. Senior Member AIAA.

Introduction

SUPERSONIC jets occur in the exhausts from rocket motors and in various other situations. When the jets impinge on solid objects, such as part of a missile launcher or the ground surface, which is of prime interest here, high-temperature and severe pressure loads can be exerted. Although the impingement flows are generally found to be extremely complex, the key feature of the jet flow is a plate shock near the opposing wall. Between the plate shock and the solid surface is a region of subsonic and transonic flows similar to the shock layer produced by a blunt body in supersonic flow. Study of the jet and its structure has been conducted for many years both experimentally[1–12] and numerically.[13–20] To cite a few among those, Kitamura and Iwamoto[17] studied supersonic jet impingement using axi-symmetric assumptions. Sakakibara and Iwamoto[18] also investigated the oscillation mechanism of the underexpanded jet impinging on a plate. They showed flowfields for different nozzle–plate distances, uncovering pressure oscillation, frequency, and separation bubble. Hong and Lee[19] presented numerical simulations of jet plume impingement onto an L-type duct using Navier–Stokes equations. Lee et al.[20] also gave numerical solutions of a vertical launcher involving supersonic jet impingement. One of the most complex applications of jet impingement in regard to missile launchers is the vertical launching system (VLS), where flow patterns are extremely complex and shown to be difficult to obtain numerical solutions.[21]

In the current work, dependency of jet impingement flow structure on the nozzle–plate distance was examined, while the other parameters were fixed. Determination of the plenum height in the VLS design was the major uncertainty because the other parameters were pretty much fixed by system specification. In the course of VLS design, it was hoped that computational fluid dynamics (CFD) analysis would provide key parameters in the industrial manufacturing process, helping structural designers with visual flow pattern as well as flow variables. In the course of the analysis, computed wall pressure is found to oscillate continuously with respect to a mean value even

after it has reached a steady state. This has become a source of interest as well as concern in terms of validity in using a steady-state code. Because the steady-state version with variable Courant–Friedrichs–Lewy (CFL) number is quite helpful in reducing the computational turn-around time to provide timely data for the system engineers, attention is paid to see how accurately solutions of steady-state code are reproducible compared to solutions of an unsteady version of the code. A validation case was added to show the accuracy of present method against a well-known experiment.[8] VLS flow was then computed, yielding necessary flow information for system designers and manufacturers. Maximum pressure location, its level, and pressure force on the bottom and the side wall were needed. The temperature, shear stress, and heat flux were also needed in choosing the ablative material and the thickness of it. A save of 1 in. of ablative material on the direct plume-hit area is worth a million dollars, considering total production.

Objectives of present work are, thus, twofold: One objective is to develop a computational tool that will capture the oscillating plate shock overcoming the numerical shock instability and to devise a time-accurate unsteady version of it to uncover the oscillating pressure mechanism, the other is to capture the jet impingement flow structure and to obtain design variables essential for VLS design.

Numerical Methods

The characteristic flux-difference splitting (CFDS) numerical method for the three-dimensional Navier–Stokes has been updated, applied to various complex flows, and validated over the past few years.[22] The CFDS method shares common flux-difference ideas with those in Refs. 23 and 24. Here a brief description is given; details may be found in Ref. 22. The governing Navier–Stokes equations employed in the generalized coordinate system, ξ, η, ϕ, are expressed for the conservative variable vector as

$$\boldsymbol{J}^{-1}\frac{\partial \boldsymbol{Q}}{\partial t}+\frac{\partial}{\partial \xi}(\hat{\boldsymbol{F}}+\hat{\boldsymbol{F}}_v)+\frac{\partial}{\partial \eta}(\hat{\boldsymbol{G}}+\hat{\boldsymbol{G}}_v)+\frac{\partial}{\partial \phi}(\hat{\boldsymbol{H}}+\hat{\boldsymbol{H}}_v)=0 \tag{1}$$

The inviscid fluxes are linearized and split for upwind discretization by

$$\Delta_\xi \hat{\boldsymbol{F}}=\tilde{\boldsymbol{A}}\Delta\boldsymbol{Q}=(\tilde{\boldsymbol{A}}^+ +\tilde{\boldsymbol{A}}^-)\Delta\boldsymbol{Q}, \qquad \tilde{\boldsymbol{A}}^\pm=\bar{\boldsymbol{M}}\bar{\boldsymbol{T}}\bar{\boldsymbol{\Lambda}}^\pm\bar{\boldsymbol{T}}^{-1}\bar{\boldsymbol{M}}^{-1} \tag{2}$$

yielding

$$\boldsymbol{J}^{-1}\frac{\delta \boldsymbol{Q}}{\Delta t}+\tilde{\boldsymbol{A}}^+\nabla_\xi \boldsymbol{Q}^{n+1}+\tilde{\boldsymbol{A}}^-\Delta_\xi \boldsymbol{Q}^{n+1}+\tilde{\boldsymbol{B}}^+\nabla_\eta \boldsymbol{Q}^{n+1}$$
$$+\tilde{\boldsymbol{B}}^-\Delta_\eta \boldsymbol{Q}^{n+1}+\tilde{\boldsymbol{C}}^+\nabla_\phi \boldsymbol{Q}^{n+1}+\tilde{\boldsymbol{C}}^-\Delta_\phi \boldsymbol{Q}^{n+1}=0 \tag{3}$$

where $\delta\boldsymbol{Q}=\boldsymbol{Q}^{n+1}-\boldsymbol{Q}^n$ and the overbar means the associated variable is space averaged over the interval $[j, j+1]$. $\bar{\boldsymbol{M}}$ or $\bar{\boldsymbol{M}}^{-1}$ is a transformation matrix between the conservative variable vector $\boldsymbol{Q}$ and the primitive variable vector $\tilde{\boldsymbol{Q}}$. $\bar{\boldsymbol{T}}$ or $\bar{\boldsymbol{T}}^{-1}$ is a transformation matrix between the primitive variable vector $\tilde{\boldsymbol{Q}}$ and the characteristic variable vector $\tilde{\tilde{\boldsymbol{Q}}}$.

The strength of current CFDS formulation is to enable one to switch the difference equation from the conservation form

$$(\boldsymbol{J}^{-1}/\Delta t)\delta\boldsymbol{Q}+\bar{\boldsymbol{M}}\bar{\boldsymbol{T}}\bar{\boldsymbol{\Lambda}}^\pm\bar{\boldsymbol{T}}^{-1}\bar{\boldsymbol{M}}^{-1}\Delta\boldsymbol{Q}=0 \tag{4}$$

to characteristic form

$$(\boldsymbol{J}^{-1}/\Delta t)\delta\tilde{\tilde{\boldsymbol{Q}}}+\bar{\boldsymbol{\Lambda}}\Delta\tilde{\tilde{\boldsymbol{Q}}}=0 \tag{5}$$

rather easily, written here for one-dimensional case for simplicity. When the eigenvalue becomes zero in Eq. (5), there is no convective wave information traveling to that point as occurs in the stagnation line. Because the CFDS formulation also splits the eigenvalue as

$$\boldsymbol{\Lambda}=\boldsymbol{\Lambda}^+ +\boldsymbol{\Lambda}^- \tag{6}$$

this splitting is also susceptible to carbuncle problem[25–29] when $\boldsymbol{\Lambda}$ becomes zero. Thus, it is necessary to prevent the eigenvalue component from becoming zero. This has been done via

$$\lambda=\lambda^+ +\lambda^-=(\lambda^+ +\varepsilon)+(\lambda^- -\varepsilon) \tag{7}$$

with a proper choice of ε. An alternative formulation for the flux term, instead of Eq. (2), to cure the shock instability is now proposed:

$$\Delta_\xi \hat{\boldsymbol{F}}=Fl_{\frac{1}{2}}-Fl_{-\frac{1}{2}} \tag{8}$$

where

$$Fl_{\frac{1}{2}}=\tfrac{1}{2}[F_j-F_{j+1}-|\tilde{\boldsymbol{A}}|(\boldsymbol{Q}_{j+1}-\boldsymbol{Q}_j)] \tag{9}$$

Here $\tilde{\boldsymbol{A}}$ is the same as in Eq. (2). The last term in Eq. (9), $|\tilde{\boldsymbol{A}}|(\boldsymbol{Q}_{j+1}-\boldsymbol{Q}_j)$, represents numerical dissipation and $|\tilde{\boldsymbol{A}}|=\bar{\boldsymbol{M}}\bar{\boldsymbol{T}}|\bar{\boldsymbol{\Lambda}}|\bar{\boldsymbol{T}}^{-1}\bar{\boldsymbol{M}}^{-1}$. The flux definition in Eq. (9) is very similar in form to Roe's flux definition. In the present study for supersonic jet impingement, and also for general use, the entropy fixing[29] for $\boldsymbol{\Lambda}$ in Eq. (9) is adopted as

$$|\boldsymbol{\Lambda}|=\{(\lambda^2+\varepsilon^2)/2\varepsilon\} \tag{10}$$

if $|\lambda|<\varepsilon$, with $\varepsilon=$ constant. This entropy fixing is used in the region where grid-aligned normal shock is detected. However, the original formulation in Eq. (2) is used for all other grid points.

Algebraic equations for $\delta\boldsymbol{Q}$ can be obtained by arranging Eq. (3) in implicit form:

$$\big[(1/\boldsymbol{J})(\boldsymbol{I}/\Delta t)+\tilde{\boldsymbol{A}}^+\nabla_\xi+\tilde{\boldsymbol{A}}^-\Delta_\xi+\tilde{\boldsymbol{B}}^+\nabla_\eta+\tilde{\boldsymbol{B}}^-\Delta_\eta$$
$$+\tilde{\boldsymbol{C}}^+\nabla_\phi+\tilde{\boldsymbol{C}}^-\Delta_\phi\big]\delta\boldsymbol{Q}=\text{RHS} \tag{11}$$

where the right-hand side (RHS) is given as

$$\text{RHS}=-\big(\tilde{\boldsymbol{A}}^+\nabla_\xi\boldsymbol{Q}^n+\tilde{\boldsymbol{A}}^-\Delta_\xi\boldsymbol{Q}^n+\tilde{\boldsymbol{B}}^+\nabla_\eta\boldsymbol{Q}^n+\tilde{\boldsymbol{B}}^-\Delta_\eta\boldsymbol{Q}^n$$
$$+\tilde{\boldsymbol{C}}^+\nabla_\phi\boldsymbol{Q}^n+\tilde{\boldsymbol{C}}^-\Delta_\phi\boldsymbol{Q}^n\big)$$

An approximate way of solving Eq. (11) is to adopt diagonally dominant alternating direction implicit approximate factorization:

$$\big(-\tilde{\boldsymbol{A}}^+_{j-1},\tilde{\boldsymbol{D}},\tilde{\boldsymbol{A}}^-_j\big)D^{-1}\big(-\tilde{\boldsymbol{B}}^+_{k-1},\tilde{\boldsymbol{D}},\tilde{\boldsymbol{B}}^-_k\big)D^{-1}\big(-\tilde{\boldsymbol{C}}^+_{l-1},\tilde{\boldsymbol{D}},\tilde{\boldsymbol{C}}^-_l\big)\delta\boldsymbol{Q}$$
$$=\text{RHS} \tag{12}$$

where

$$\tilde{\boldsymbol{D}}=(1/\boldsymbol{J}\Delta t)\boldsymbol{I}+\tilde{\boldsymbol{A}}^+_{j-1}-\tilde{\boldsymbol{A}}^-_j+\tilde{\boldsymbol{B}}^+_{k-1}-\tilde{\boldsymbol{B}}^-_k+\tilde{\boldsymbol{C}}^+_{l-1}-\tilde{\boldsymbol{C}}^-_l$$

where $\delta\boldsymbol{Q}$ can be obtained by three-stage calculation from

$$\big(-\tilde{\boldsymbol{A}}^+_{j-1},\tilde{\boldsymbol{D}},\tilde{\boldsymbol{A}}^-_j\big)\delta\boldsymbol{Q}^{**}=\text{RHS}$$
$$\big(-\tilde{\boldsymbol{B}}^+_{k-1},\tilde{\boldsymbol{D}},\tilde{\boldsymbol{B}}^-_k\big)\delta\boldsymbol{Q}^{*}=\tilde{\boldsymbol{D}}\delta\boldsymbol{Q}^{**}$$
$$\big(-\tilde{\boldsymbol{C}}^+_{l-1},\tilde{\boldsymbol{D}},\tilde{\boldsymbol{C}}^-_l\big)\delta\boldsymbol{Q}=\tilde{\boldsymbol{D}}\delta\boldsymbol{Q}^{*} \tag{13}$$

Upwind flux-difference splitting for the inviscid fluxes and second-order central differencing for the viscous fluxes are applied for the discretization. The viscous terms are treated explicitly in Eq. (13) through RHS. To simulate unsteady flow, inner iteration time terms are added to Eq. (13). This dual-time-step method[30] is implemented through adding terms in diagonal $\tilde{\boldsymbol{D}}$ and RHS as follows:

$$\tilde{\boldsymbol{D}}=(1/\boldsymbol{J})[(1+\alpha/2)(1/\Delta t)+1/\Delta\tau]\boldsymbol{I}+\tilde{\boldsymbol{A}}^+_{j-1}-\tilde{\boldsymbol{A}}^-_j$$
$$+\tilde{\boldsymbol{B}}^+_{k-1}-\tilde{\boldsymbol{B}}^-_k+\tilde{\boldsymbol{C}}^+_{l-1}-\tilde{\boldsymbol{C}}^-_l \tag{14}$$

$$\text{RHS}=-(1/\boldsymbol{J})\{(1+\alpha/2)[(\boldsymbol{Q}^l-\boldsymbol{Q}^n)/\Delta t]$$
$$-(\alpha/2)(\Delta\boldsymbol{Q}^{n-1}/\Delta t)\}+\text{RHS}^l \tag{15}$$

where RHS^l is the same as RHS in Eq. (12), $\alpha = 1$ for second-order in time, $\Delta\tau$ is the physical time, and Δt represents subiteration.

For the turbulent flow effect, the Baldwin–Lomax[31] model is employed primarily. For application to more complex flow situation, one-equation models of Spalat–Allmaras[32] and of Baldwin–Barth[33] are added as options. Basically, the following sections address the issue of convergence especially in view of highly fluctuating nature of pressure at the wall.

Results and Discussion

Jet Impingement onto Flat Plate Using a Test Motor

Supersonic jet impingement with a small test motor is run for a chamber condition of pressure $P_t = 82.7 \times 10^5$ Pa (1200 psia) and temperature $T_t = 2950$ K. The three main parameters are Mach number at the nozzle exit plane, the pressure ratio P_r between the jet exit plane and the ambient, and the distance between the nozzle and the wall. The pressure ratio is 1.87, the nozzle exit Mach is 2.93, and the height H is made variable. Figure 1 shows the jet impingement layout with the nozzle diameter of $D = 3.26$ cm and the nozzle–plate spacing H. For the present problem, the computational grid consists of 310,000 grid points and of 7 blocks. The first grid off the wall is about $y+ = 1$, and there are five grid points below $y+ = 10$. This is to ensure accurate heat transfer calculations to be used as input for ablation prediction. Also an overlap grid technique is used at block interfaces to exchange data. The boundary conditions at the nozzle throat are calculated from isentropic relations and perfect gas law, knowing the chamber pressure and temperature. The computational domain starts from the nozzle throat with a Mach 1.0 condition. It is our experience for nozzle flow computations involving a live motor that the static pressure in the jet and the wall pressure, if the jet hits a surface, have been reproduced accurately with ideal gas flow computations despite the high-temperature environment. The temperature, however, is found to be slightly different from the measurement.

The jet impinging distance H is varied incrementally from $3D$, $4D$, $5D$, to $6D$ to illuminate the characteristics of the jet plume with the distance, while P_r is fixed at 1.87. When a supersonic jet plume exhausts against the plate, a strong normal shock is formed above the plate. If the grid system used for computation is aligned with this normal shock, as is the case here, the shock instability occurs that can be cured by modifying eigenvalues through numerical dissipation terms in the flux. Figure 2 shows Mach contours in a symmetric plane contaminated with a shock instability, the so-called carbuncle phenomenon. After treatment of the eigenvalue as modified in Eq. (9), stable solutions are obtained as shown in Fig. 3, displaying Mach contours with shock shell, plate shock, and Mach disk for various H. As the distance H increases, the shock structures are also stretched, but the first shock shell and the distance between the wall and standing plate shock remain nearly the same. Pressure contours on the wall are also presented in Fig. 3b, corresponding to $H = 4D$. Wall pressure contours form exact circles in spite of using the rectangular grid in the core zone; a tribute to the numerically robust scheme.

Figure 4 shows a comparison of pressure histories as a function of numerical iterations. The unsteady nature of wall pressure fluctuations due to bouncing of the plate shock is noticed for a strong pressure ratio of 1.87. As the plate is placed closer to the nozzle,

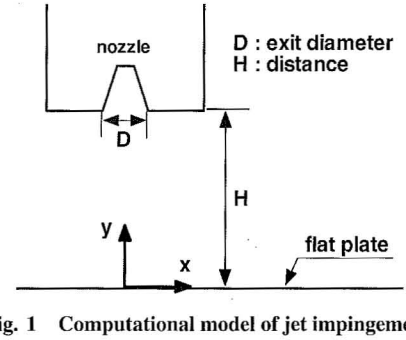

Fig. 1 Computational model of jet impingement.

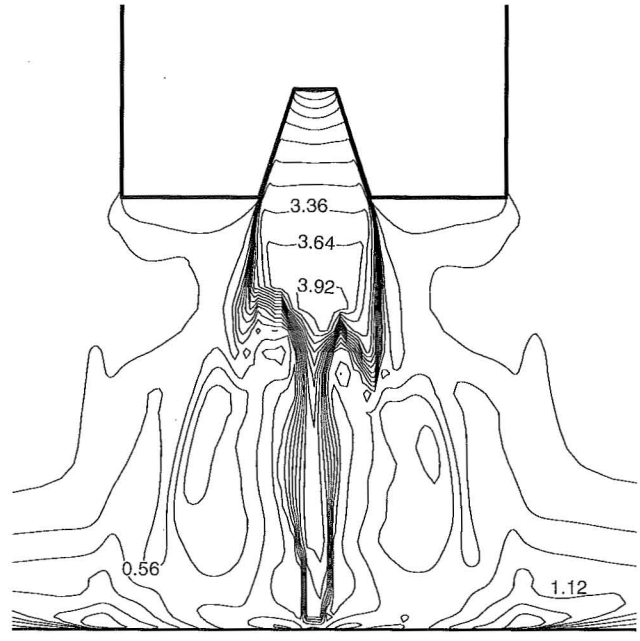

Fig. 2 Mach contours in symmetric plane without eigenvalue fixing.

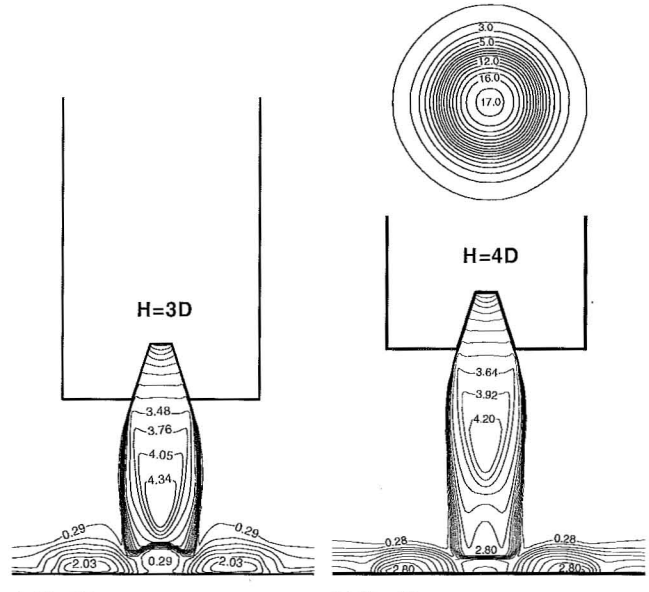

a) $H = 3D$ b) $H = 4D$

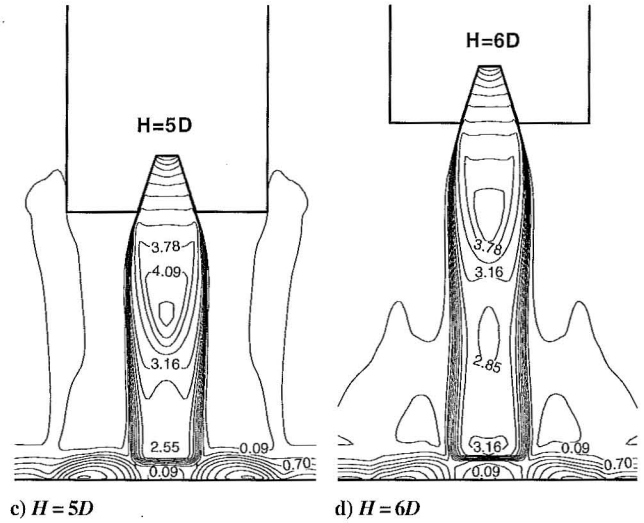

c) $H = 5D$ d) $H = 6D$

Fig. 3 Mach contours in symmetric plane for various heights H and wall pressure contours b relative to ambient pressure for $H = 4D$.

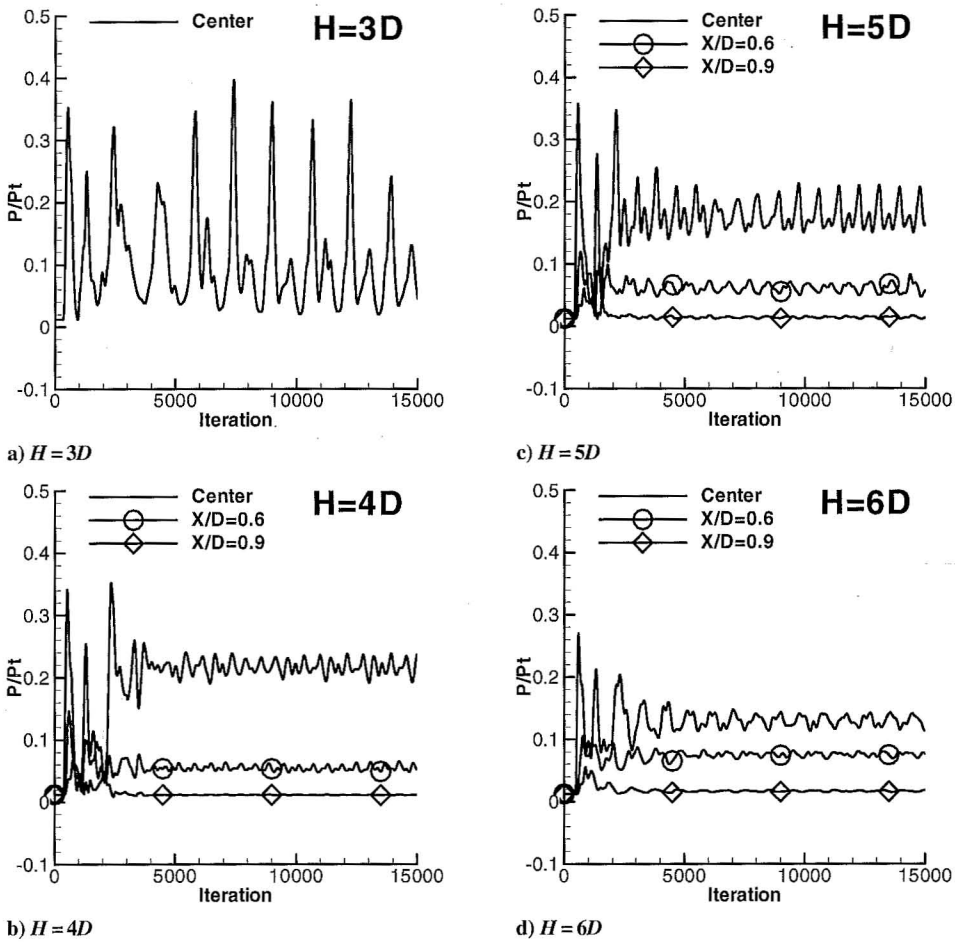

Fig. 4 Pressure histories for different heights of H.

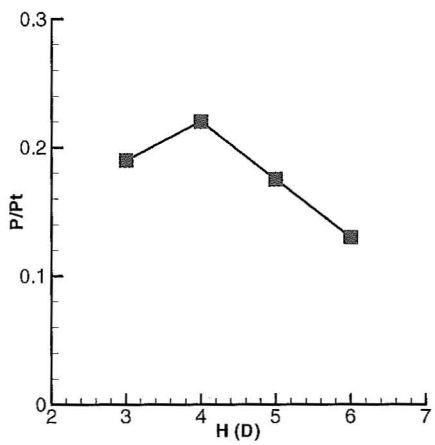

Fig. 5 Wall pressure variation at the jet center as a function of height H.

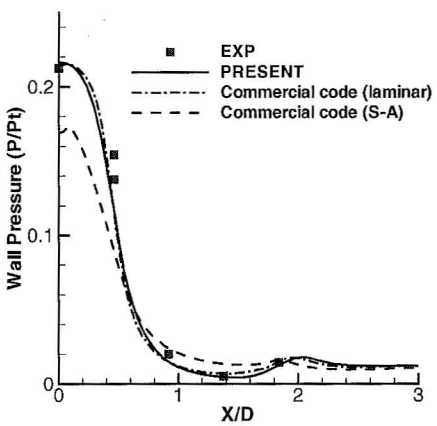

Fig. 6 Comparison of wall pressure distributions in radial direction for $H = 4D$ case.

the pressure fluctuates more vigorously and oscillates with large amplitude with respect to the mean value as in the $H = 3D$ case. The wall pressure becomes quiet as it moves away from the center, for example, at $X/D = 0.9$ in Fig. 4. As the nozzle is moved farther away from the plate, the maximum Mach just before the Mach disk decreases from 4.34 to 3.78, as in Fig. 3, which means that the flow accelerates faster with more energy for $3D$ case than for $6D$ case. However, the faster and harder the flow pushes against the wall, the stronger the reaction becomes off the wall, thereby creating the violent pressure fluctuations as observed in Fig. 4. The amplitude of wall pressure fluctuations subsides as the distance increases; the frequency is estimated as on the order of 1–10 kHz. The maximum mean pressure level at the plate is achieved when the distance is about $4D$ high, as shown in Fig. 5 as a function of height. The mean pressure is obtained after the solution has reached its steady state.

The computed wall pressure variation in the radial direction is compared against an experimental data set and the numerical results obtained from one of the popular commercial codes with laminar and turbulent flow options in Fig. 6 for the $H = 4D$ case. The comparison is generally good between the computation and the measurement, except for the commercial code run with the Spalart–Allmaras model. Both the computed and experimental data are averaged in the steady-state period. Pressure distribution in the radial direction in Fig. 6 shows a typical pattern for a supersonic jet impinging on a flat plate with the single peak at the jet center. Depending on H and P_r, double-peak pressure distribution can occur, to be shown later. The

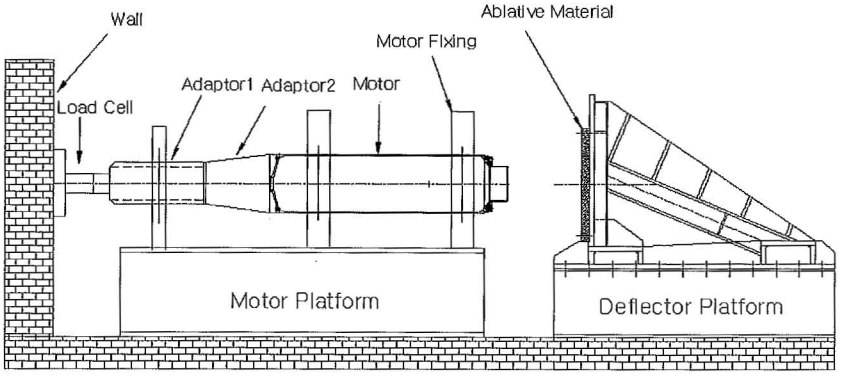

Fig. 7 Experimental setup for jet impingement.

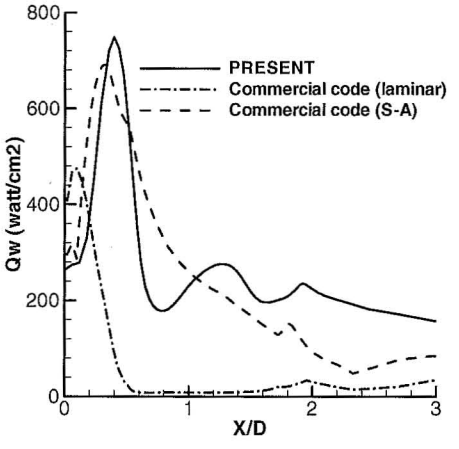

Fig. 8 Comparison of heat flux distributions in radial direction for $H = 4D$ case.

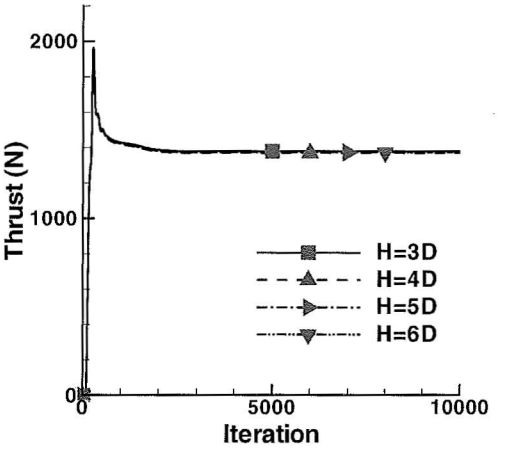

Fig. 9 Thrust history comparisons for various distance H.

measurement apparatus as shown in Fig. 7 was designed specifically for the present purpose of validation and was carried out by expert team at the Agency for Defense Development with the accuracy within 5%. Pressure and temperature sensors are located on the flat plate with seven pressure holes and four temperature gauges. This experiment was done solely to provide the database for our computation and to measure the wall erosion for the ablative material.

Heat flux distribution in radial direction is also deduced in Fig. 8 for $4D$ case, reaching its maximum value at about $X/D = 0.4$. Although the laminar flow solution shown in Fig. 6 gave a good comparison with the experimental trend, its heat flux prediction is quite displaced from turbulent flow computations. This demonstrates the inadequacy of laminar flow calculation for this highly viscous flow, although the pressure was determined correctly. The heat flux distribution is especially important for prediction of ablation characteristics. A separate effort was made to predict the amount and pattern of ablation for carbon–carbon material at the jet center. A rather large discrepancy was resulted in the initial stage of work, which was refined with a trial-and-error approach based on measurement data. The calculated thrust for various distances yields the same value in Fig. 9, reaching a steady-state value of 1423 N after 3000 iterations. The convergence of nozzle thrust to a constant value means that the flow structure inside the nozzle is independent of the distance between the exit and the plate beyond $3D$ height.

Accuracy of the forgoing results and the occurrence of double-peak structure are also indirectly verified from computing the experimental flow of Lamont and Hunt,[8] where the exit Mach is 2.2, the pressure ratio is 1.2, and the nozzle–plate distances are $0.5D$ and $3.0D$. Comparisons in Figs. 10 and 11 show reasonable matches between the computed and the experiment. The central code in Fig. 11 represents results of an in-house code employing central-difference flux-vector splitting method. The double-peak pressure distribution is also captured in Fig. 11b, where the double-peak pressure implies existence of recirculation of the flow trapped in the subsonic zone.

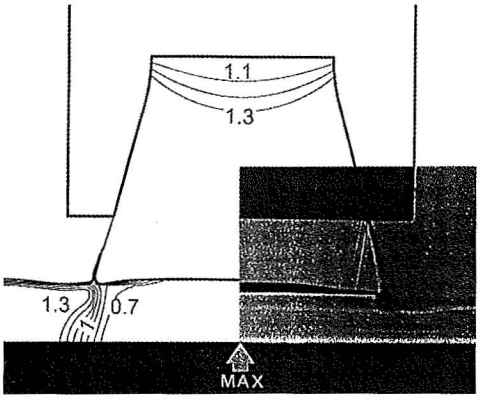

Fig. 10 Comparison of computed Mach contours for $H = 0.5D$ with shadowgraph taken from Lamont and Hunt.[8]

Jet Impingement onto Flat Plate Using Full-Scale Motor

A second full-scale motor with chamber pressure of 103.3×10^5 Pa (1500 psia), exit Mach of 2.93, temperature of 2970 K, and nozzle diameter of 18.2 cm was computed. The pressure ratio is 2.33, and the height H is $7.34D$. Many runs were made to show the dependency of jet impingement structure on height with this motor, but because the purpose is to find the acceptable level of pressure and heat transfer rate at the center of the impinging wall, it was found that the current height of $7.34D$ has a marginal level of pressure and heat load in view of space constraints (mainly, height) of the vertical launcher to be discussed in the next section. When the nozzle–plate distance is decreased from $7.34D$ to $5.0D$, for example, the heat flux increases by 2.5 times and the pressure by 1.5 times.

Another point of simulation is to see whether the unsteady behavior of pressure near the jet center observed with the steady-state

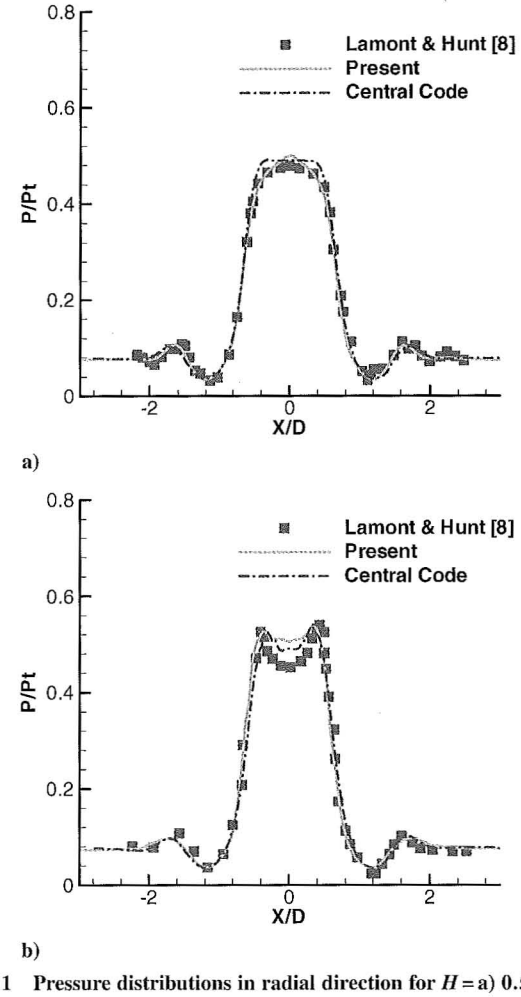

Fig. 11 Pressure distributions in radial direction for H = a) $0.5D$ and b) $3.0D$.

version can be reproduced with the unsteady simulation using a fixed time step. Thus, in this section, emphasis is placed on comparing the steady-state solutions obtained with variable CFL number with the time-accurate unsteady solutions using the inner iterations.[30] The number of grid points are 800,000 due to increased height between the nozzle and the wall. Figure 12 shows a comparison of the pressure contours, which are plotted with 0.06 interval between 0 and 3 atm, displaying good agreement between the two sets of numerical solutions. The locations of shock shells and flow structures are identical between the two sets of solutions. In comparison to those in Fig. 3, three shock shells are captured due to increased height to $7.34D$. The unsteady calculation utilizes 20 subiterations. Figure 13 also shows a comparison of the convergence history of wall pressure at the center of the plate. During the initial stage of plume exhaust, the steady code solutions display more violent behavior than the unsteady code solutions, but overall the two solutions converge to the same value of 14.5 atm. Convergence of wall pressures to this identical value between the steady-state code and the unsteady code solutions gave confidence in this computation in that the majority of the engineering design was done by the steady-state code and the steady-state code with variable CFL is proven to be viable in capturing the physically meaningful solutions even when the solution (pressure) keeps fluctuating with respect to a mean value. It is observed that the seemingly steady-state pressure still oscillates regularly when the pressure history is magnified, as in Fig. 13a. The oscillation frequency is found to be 2.8 kHz, which is slightly lower than the ones corresponding to those in Fig. 4, where the present case has greater height between the nozzle and the wall.

Jet Impingement Structure

Figure 14a is a plot of typical shock structure in the jet impingement onto flat plate. Figure 14b shows Mach disk locations ob-

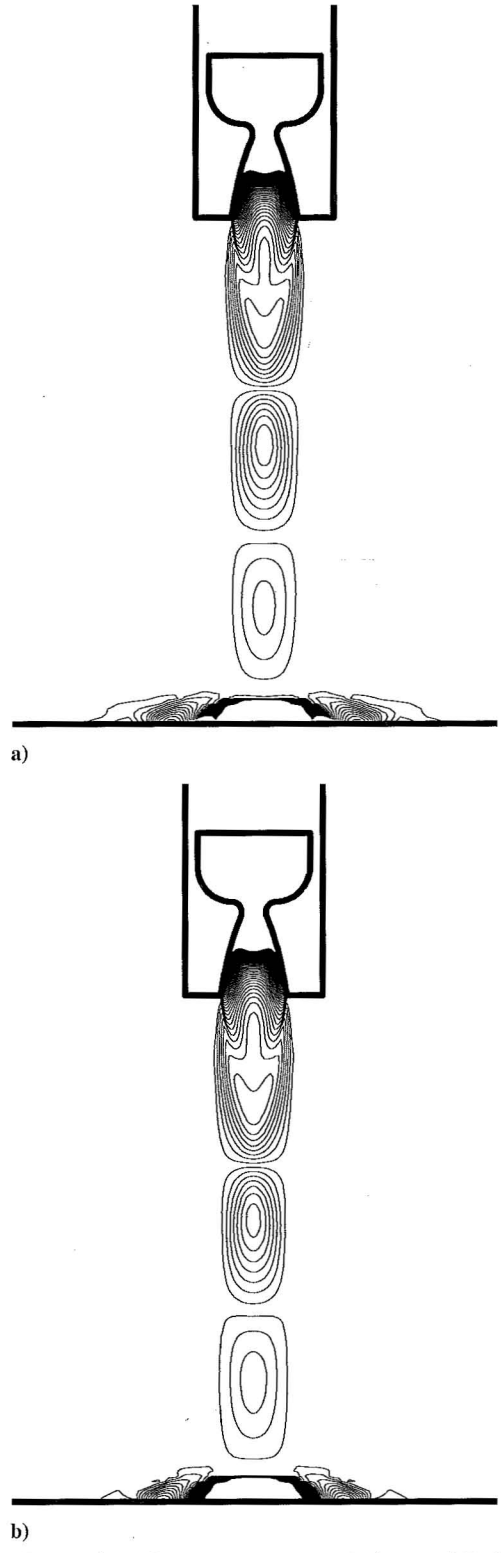

Fig. 12 Comparison of pressure contours solutions at $\Delta P = 0.06$ atm between a) unsteady code and b) steady code.

tained from current computations against the distance away from the nozzle exit. The locations of the disks within the jet boundary are denoted by $Y1$, $Y2$, and Ys in Fig. 14a. When the nozzle-to-plate distance Y/D is greater than 3.0, at least single shock shell is formed above of the plate. As the plate is moved further from the nozzle exit ($Y/D > 3.0$), the plate shock moves together with the plate. The distance between the plate and the plate shock (Y–Ys) is almost independent of the nozzle-to-plate distance. The size of the first cell or the second cell depends on the jet pressure ratio, but it remains fixed once the pressure ratio is fixed. In Fig. 14b, Mach

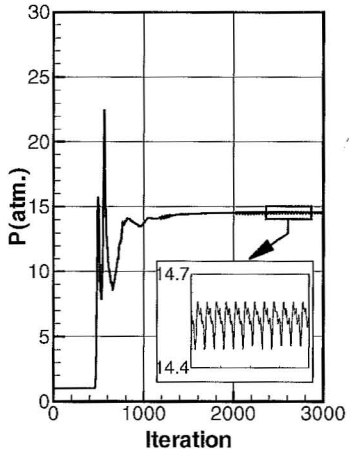

a)

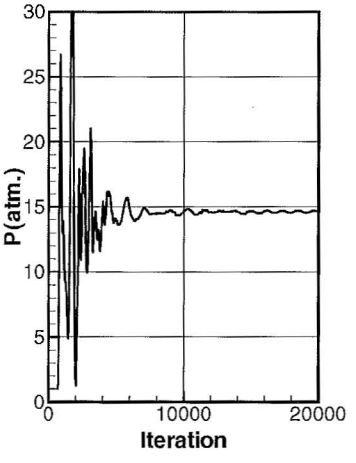

b)

Fig. 13 Pressure history solutions comparison between a) unsteady and b) steady code.

disk locations obtained from computations of test motor as well as full-scale motor of previous sections are collected, showing the same length of each shock shell between the two cases and constant shock stand-off distance. The length of the first three shock shells is plotted in Fig. 14c in terms of shock shell number, showing almost a linear decrease but showing presence of wall on the third shell.

Jet Impingement in VLS

The VLS is a ship-based missile launcher, which consists of several launch canisters containing missiles, which are installed below the ship's deck. The primary concern of VLS design is the optimization of scales associated with the plenum and uptake to allow safe exhaust of jet plume. Before fixing the scale, the plenum height and uptake width are considered to be variable and left for CFD flow analysis. The same computational methodology as in the flat plate impingement in terms of grid topology, grid density, and numerical scheme with λ correction is then applied to the VLS where the jet plume hits the bottom wall, is deflected into the plenum, and eventually exits through the vertical uptake. The uptake is a long rectangular duct.

For computation, the grid topology is constructed as shown in Fig. 15 with 1.8 million grid points. A circular grid is adopted where canister is placed as shown in Figs. 15a and 15b, and the overall computational grid system is shown in Fig. 15c. The pressure ratio P_r is 2.33, and H is $7.34D$, the same as in the preceding full-scale motor.

Computation revealed that the wall pressure goes up as high as 20 times that of the ambient pressure at the center of the plume-hitting cell. VLS results are presented in Figs. 16 and 17 at selected planes. Mach contours of selected planes are shown in Fig. 16a for the yz-plane with a 0.1 interval, Fig. 16b for the uptake centerplane with a 0.02 interval, and Fig. 16c for the xy plane through the motor

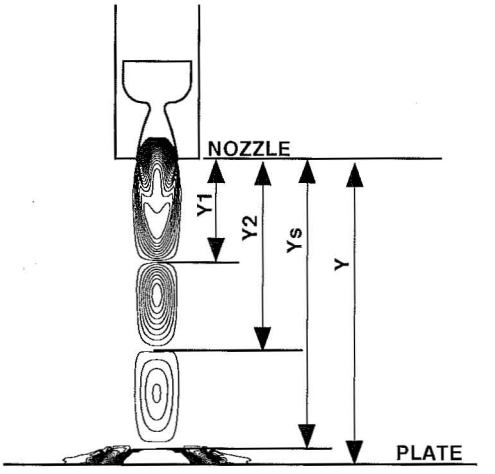

a) Shock shells

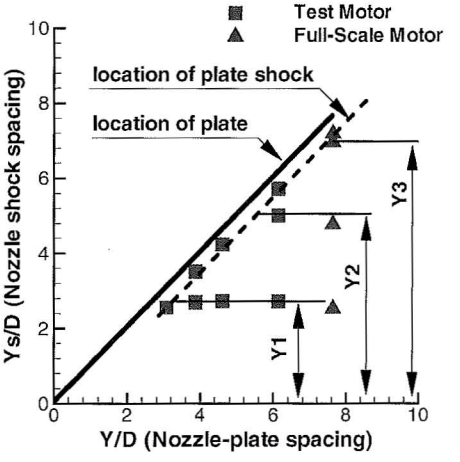

b) Mach disk locations: ■, test motor and ▲, full-scale motor

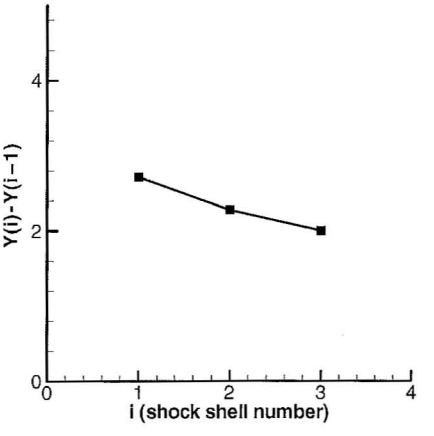

c) Variation of successive shock shell lengths

Fig. 14 Mach disk locations as a function of nozzle height.

center with a 0.1 interval. The jet plumes both in the yz plane and in the xy plane are shown to be swaying against the side wall due to the effect of the surrounding wall interference with the jet plume. These bent shock shells did not occur in the jet impingement onto the flat plate. The fluctuations of the shock shell in the horizontal plane are indicated during numerical iterations, caused by the large recirculation of flow bounced off the bottom and side walls. The jet plume exhausts through the uptake at the speed of Mach 0.6 as shown in Fig. 16b.

The pressure contours are presented in Fig. 17 for the same planes chosen in Fig. 16 and the plenum bottom. The pressure levels in plenum chamber are two to three times the atmospheric pressure except in the plume-hitting area. The pressure history at the bottom

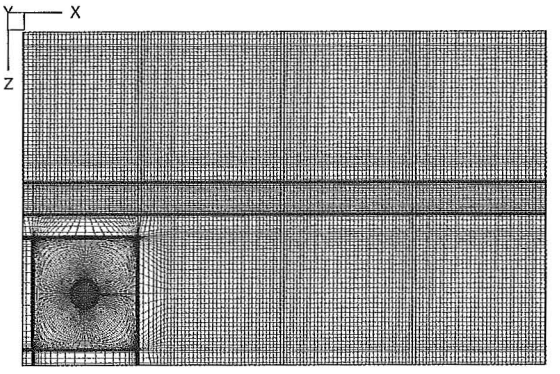

a) Plenum grid with corner motor

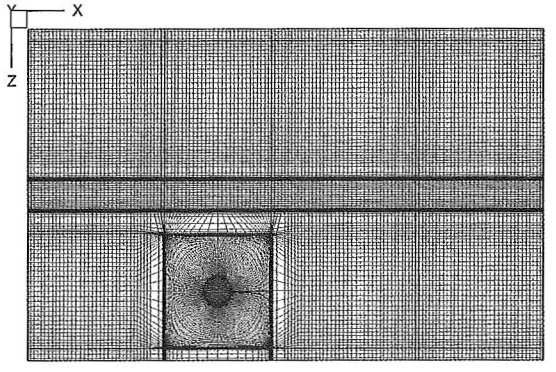

b) Plenum grid with inner motor

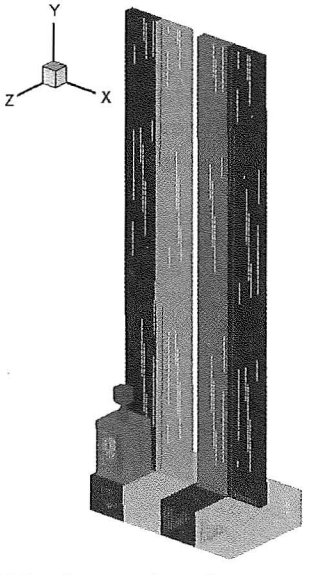

c) Surface grid for plenum and uptake

Fig. 15 Computational grid topology for VLS.

wall of the plenum center shows the unsteady nature of the plate shock, having a frequency of 7.3 kHz and a mean pressure of 10 atm. The magnitude of the peak pressure and overall pressure force impacting the bottom plate of the plenum are very essential in designing the VLS structural integrity. They are also important in choosing the ablative material and its thickness at the center of direct plume hit area. Figure 18 contains shear stress τ_w, as well as heat flux distributions along the x direction. The origin of x denotes the center of motor. The heat flux is maximum off the jet center, and the left peak is higher than the right peak due to its proximity to the side wall. The heat flux level is 280 W/cm^2, which is severe for ordinary material. The shear stress is zero at the jet center, implying the wall jet changes direction. A combination of experimental and semi-empirical approaches was carried out separately to determine the material design.

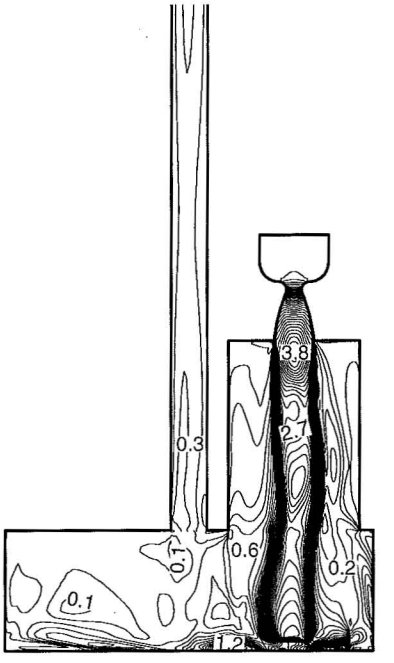

a) The yz plane view with $\Delta M = 0.1$

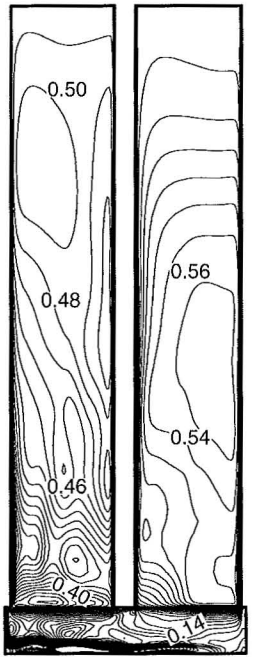

b) The xy plane view through the uptake with $\Delta M = 0.02$

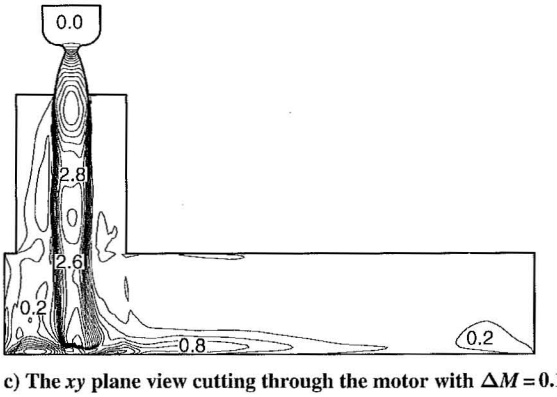

c) The xy plane view cutting through the motor with $\Delta M = 0.1$

Fig. 16 Mach contours in VLS selected planes.

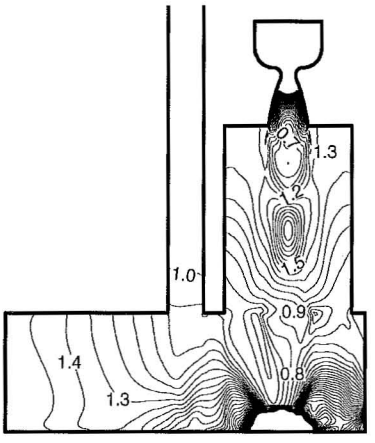

a) The *yz* plane view with $\Delta P = 0.05$

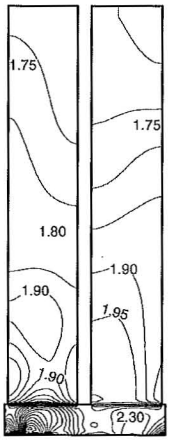

b) The *xy* plane view through the uptake with $\Delta P = 0.2$

c) The *xy* plane view cutting through the motor with $\Delta P = 0.1$

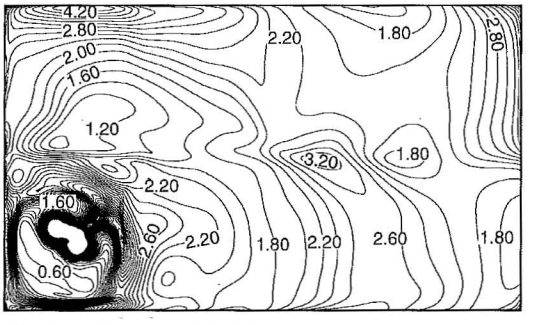

d) Plenum bottom wall with $\Delta P = 0.2$

Fig. 17 Pressure contours in VLS selected planes.

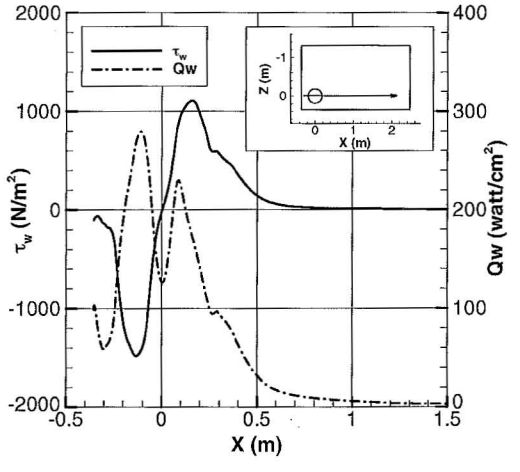

Fig. 18 Wall shear stress and heat flux on the plenum bottom along *x* coordinate.

Among other requirements, it was required to estimate the strength of the reflected jet pushing the inside of the plenum upper wall; this is where there are eight doors to handle the canisters. When calculated from the pressure field, each door faces about 70,000 or 560,000 N on the upper plenum wall. Flow structures within the VLS are, thus, visualized and solutions quoted as a few examples provide essential data for the structural design of the VLS.

Conclusions

The jet impinging flows encountered in the design of a missile system are discussed with the purpose of uncovering the physics associated with the flow and providing vital data for system engineers. The jet impingement creates the plate shock, which is difficult to capture with Roe-type flux-difference method, requiring modification of the system eigenvalue when it approaches near-zero value. Depending on the nozzle–wall distance, single- or double-peak wall pressure distribution is observed, and the unsteady nature of the plate shock along with the wall pressure fluctuation is also uncovered. Plume structures are also captured for several nozzle–wall heights.

When the plate shock oscillations are analyzed with a Fourier transform routine, they reveal a frequency range of 1–10 kHz for the flat plate jet impingement. The shock shell fluctuations in the horizontal direction are also dominated by a frequency of 7.3 kHz for the VLS internal flow. The frequency range for mechanical failure is from 1 to 10 kHz, and thus, it is important for electronic parts to avoid or withstand this frequency range during launch. The pressure, temperature, shear stress, heat flux, and jet speed within the VLS are then utilized by the system designers, demonstrating the capability of CFD at the engineering design level.

References

[1]Gummer, J. H., and Hunt, B. L., "The Impingement of a Uniform, Axisymmetric, Supersonic Jet on a Perpendicular Flat Plate," *Aeronautical Quarterly*, Vol. 12, Aug. 1971, pp. 403–420.

[2]Donaldson, C., DUP. and Snedeker, R. S., "A Study of Free Jet Impingement. Part 1. Mean Properties of Free and Impinging Jets," *Journal of Fluid Mechanics*, Vol. 45, No. 2, 1971, pp. 281–319.

[3]Knight, C. V., "Experimental Investigation of Two-Dimensional, Supersonic Flow Impingement on a Normal Surface," *AIAA Journal*, Vol. 11, No. 2, 1973, pp. 233–235.

[4]Kalghatgi, G. T., and Hunt, B. L., "Occurrence of Stagnation Bubble in Supersonic Jet Impingement Flows," *Aeronautical Quarterly*, Vol. 27, Aug. 1976, pp. 169–185.

[5]Lamont, P. J., and Hunt, B. L., "The Impingement of Underexpanded Axisymmetric Jets on Wedges," *Journal of Fluid Mechanics*, Vol. 76, Pt. 2, 1976, pp. 307–336.

[6]Zien, T. F., and Driftmyer, R. T., "Two-Dimensional Supersonic Jet Impingement on a Flat Plate," *AIAA Journal*, Vol. 17, No. 1, 1979, pp. 4–5.

[7]Pamadi, B. L., "On the Impingement of Supersonic Jet on a Normal Flat Surface," *Aeronautical Quarterly*, Vol. 33, Aug. 1982, pp. 199–218.

[8]Lamont, P. J., and Hunt, B. L., "The Impingement of Under-Expanded Jet Interaction with a Plane Obstacle," *Journal of Fluid Mechanics*, Vol. 100, No. 3, 1980, pp. 471–511.

[9]Iwamoto, J., "Impingement of Under-Expanded Jets on a Flat Plate," *Journal of Fluid Engineering*, Vol. 112, No. 2, 1990, pp. 179–184.

[10]Masuda, W., and Moriyama, E., "Aerodynamic Characteristics of Underexpanded Coaxial Impinging Jets," *JSME International Journal, Series B*, Vol. 37, No. 4, 1994, pp. 769–775.

[11]Al-Qutub, A. M., and Budair, M. O., "Experiments of the Flow over a Flat Surface Impinged by a Supersonic jet," AIAA Paper 95-2935, July 1995.

[12]Alvi, F. S., and Iyer, K. G., "Mean and Unsteady Flowfield Properties of Supersonic Impinging Jets with Lift Plates," AIAA Paper 99-1829, May 1999.

[13]Rubel, A., "Inviscid Axisymmeetric Jet Impingement with Recirculating Stagnation Regions," *AIAA Journal*, Vol. 21, No. 3, 1983, pp. 351–357.

[14]Rizk, M. H., and Menon, S., "Numerical Simulation of Impinging Jets," AIAA Paper 86-0279, Jan. 1986.

[15]Kim, K. H., and Chang, K. S., "Three-Dimensional Structure of a Supersonic Jet Impinging on an Inclined Plate," *Journal of Spacecraft and Rockets*, Vol. 31, No. 5, 1994, pp. 778–782.

[16]Chow, W. L., Ke, Z. P., and Lu, J. Q., "The Interaction between a Jet and a Flat Plate—An Inviscid Analysis," *Journal of Fluids Engineering*, Vol. 117, Dec. 1995, pp. 623–627.

[17]Kitamura, S., and Iwamoto, J., "Numerical Analysis of Supersonic Imping Jet," *Transactions of the Japan Society for Aeronautical and Space Sciences*, Vol. 41, No. 132, 1998, pp. 57–64.

[18]Sakakibara, Y., and Iwamoto, J., "Numerical Study of Oscillation Mechanism in Underexpanded Jet Impinging on Plate," *Journal of Fluids Engineering*, Vol. 120, Sept. 1998, pp. 477–481.

[19]Hong, S. K., and Lee, K. S., "Simulation of Jet Plume Impinging onto a Duct," *13th International Symposium on Air Breathing Engines*, International Society for Air Breathing Engines, Chattanooga, TN, 1997, pp. 1359–1365; also Paper ISABE 97-7184, 1997.

[20]Lee, K. S., Hong, S. K., and Park, S. O., "Internal Flow Characteristics of VLS Type Canister," *Proceedings of the First National Congress on Fluids Engineering*, Korean Society of Mechanical Engineers, Muju, Republic of Korea, 2000, pp. 511–514.

[21]Bertin, J. J., Bertin, R. S., and Yung, A., "The Launch-Tube Flow-Field for a Vertical Launching System," AIAA Paper 88-0332, Jan. 1988.

[22]Lee, K. S., Hong, S. K., and Park, S. O., "Improvement in Flux-Difference Splitting Algorithm for Accurate and Robust Flow Simulation," *Computational Fluid Dynamics Journal*, Vol. 10, No. 2, 2001, pp. 181–191.

[23]Lombard, C. K., Oliger, J., Yang, J. Y., and Davy, W. C., "Conservative Supra-Characteristics Method for Splitting the Hyperbolic Systems of Gasdynamics with Computed Boundaries for Real and Perfect Gases," AIAA Paper 82-0837, June 1982.

[24]Lombard, C. K., "Multi-Dimensional Formulation of CSCM—An Upwind Flux Difference Eigenvector Split Method for the Compressible Navier–Stokes Equations," AIAA-Paper 83-1895, July 1983.

[25]Quirk, J. J., "A Contribution to the Great Riemann Solver Debate," *International Journal for Numerical Methods in Fluids*, Vol. 18, No. 6, 1994, pp. 555–574.

[26]Sanders, R., Morano, E., and Druguet, M. C., "Multidimensional Dissipation for Upwind Schemes: Stability and Applications to Gas Dynamics," *Journal of Computational Physics*, Vol. 145, No. 2, 1998, pp. 511–537.

[27]Liou, M. S., "Mass Flux Schemes and Connection to Shock Instability," *Journal of Computational Physics*, Vol. 160, No. 2, 2000, pp. 623–648.

[28]Pandolfi, M., and D'ambrosio, D., "Numerical Instabilities in Upwind Methods: Analysis and Cures for the 'Carbuncle' Phenomenon," *Journal of Computational Physics*, Vol. 166, No. 2, 2001, pp. 271–301.

[29]Harten, A., "High Resolution Schemes for Hyperbolic Conservation Laws," *Journal of Computational Physics*, Vol. 49, No. 3, 1983, pp. 357–393.

[30]Matsuno, K., "A Time-Accurate Iterative Scheme for Solving the Unsteady Compressible Flow Equations," AIAA Paper 89-1992, June 1989.

[31]Baldwin, B., and Lomax, H., "Thin Layer Approximation and Algebraic Model for Separated Turbulent Flows," AIAA Paper 78-257, Jan. 1978.

[32]Spalart, P. R., and Allmaras, S. R., "A One-Equation Turbulence Model for Aerodynamic Flows," AIAA Paper 92-0439, Jan. 1992.

[33]Baldwin, B. S., and Barth, T. J., "A One-Equation Turbulence Transport Model for High Reynolds Number Wall-Bounded Flows," AIAA Paper 91-0610, Jan. 1991.

R. M. Cummings
Associate Editor